energies

MDPI

Article

Spatiotemporal Evolution and Fluctuation Characteristics of a Centrifugal Compressor under Near-Stall Conditions and High Mass-Flow Rate

Kang Xiao, Zhengdao Wang, Hui Yang and Yikun Wei *

Key Laboratory of Fluid Transmission Technology of Zhejiang Province, Zhejiang Sci-Tech University, Hangzhou 310018, China
* Correspondence: yikunwei@zstu.edu.cn

Abstract: Spatiotemporal evolution and fluctuation characteristics of a centrifugal compressor are investigated by numerical simulation under near-stall conditions and with a high mass-flow rate. The large-eddy simulation (LES) for unsteady computations is implemented in the numerical simulation of unsteady flow. The internal flow physical mechanism of the centrifugal compressor is presented at a high mass-flow rate (1.1 Qn) and low mass-flow rate (0.8 Qn, near-stall). The spatiotemporal evolution of the velocity and streamline for the internal flow of the centrifugal compressor demonstrates that a lot of large-scale eddies near the tongue are transformed into small-scale ones at high mass-flow rates. High mass-flow rate resulted in excessive fluid velocity in the impeller. A large amount of impact loss massive backflow appears near the tip clearance, and boundary layer separation of the suction surface emerges firstly and at a low mass-flow rate. Considerable flow loss occurs in the centrifugal compressor at the two non-designed operating flow rates. Several pressure and velocity fluctuations in the key position of the compressor are presented by the two deviations from design conditions. The analysis of the fast Fourier transform (FFT) and amplitude spectrum show that the starting point of flow instability in the impeller is different for the two deviations from design-condition flow rates. Understanding the spatiotemporal evolution and spatiotemporal characteristics of pressure and velocity fluctuations can provide insight into the unsteady internal flow of centrifugal compressors at high mass-flow rates (1.1 Qn) and near-stall conditions (0.8 Qn).

Keywords: centrifugal compressor; vaneless diffuser; large-eddy simulation; fast Fourier transform

Citation: Xiao, K.; Wang, Z.; Yang, H.; Wei, Y. Spatiotemporal Evolution and Fluctuation Characteristics of a Centrifugal Compressor under Near-Stall Conditions and High Mass-Flow Rate. *Energies* **2023**, *16*, 84. https://doi.org/10.3390/en16010084

Academic Editors: Gabriela Huminic and Jian Liu

Received: 1 November 2022
Revised: 6 December 2022
Accepted: 15 December 2022
Published: 21 December 2022

1. Introduction

Centrifugal compressors are widely used in heavy industries (e.g., petrochemicals and aerospace), construction equipment, and household appliances. As a complex and extensively used rotating machine, centrifugal compressors are characterized by excellent efficiency and wide operating conditions [1–4]. The range of stable operating conditions has been studied to understand the operating mechanisms of centrifugal compressors in order to increase work efficiency and operational stability of the deviated design. Under non-designed working conditions, complex unsteady flow structures caused by the rotating Coriolis force and the exacerbation of the boundary layer by narrow-blade passage play a dominant role in affecting energy losses of centrifugal compressors.

That energy loss changes velocity was proposed by Fowler et al. [1]. High and low mass-flow rates exist in different flow stall mechanisms. Backflow is caused at the tip clearance and the boundary layer of the impeller at a low mass-flow rate, which leads to the rotating stall of centrifugal compressors. Iwakiri et al. [2] described how the loss of secondary flow generates pressure fluctuations. Kim et al. [3] proposed that the flow field appears disordered near chocks. The study developed insights into the understanding of a high mass-flow rate's physical mechanism. Fluid velocity is excessive in the impeller, bringing a large amount of impact loss and increasing vortex separation near the tongue.

Based on the above discussions, the efficiency is relatively low at both non-designed working conditions, and these complex flow mechanisms may bring about safety accidents with centrifugal compressors.

Tomita et al. [5] found that pressure fluctuation for a small range of operating conditions is likely to cause rotational stall, while a large range of operating conditions is more conducive to a stabilized flow field. At this stage, unsteady flow of centrifugal compressors has mainly been studied in the context of a low mass-flow rate. Cao et al. [6] discovered flow instability in the impeller machinery. Emmons et al. proposed the circumferential propagation mechanism of the stalled group. Dodds et al. [7] further explained the rotating stall mechanism at high speeds. The airflow angle of a channel did not match the blade inlet angle, which affected the stall development of adjacent channels. Jenny et al. [4] noted that the stall theory had been widely used. In the study of stall phenomenon in an axial compressor, Fujisawa et al. [8] proposed that tip clearance flow and impeller wake flow cause rotational stall in compressors. Pascale et al. [9] confirmed that wake and blade-runner interactions lead to flow instability. Everitt et al. [10] believed that the diffuser is closely related to the rotating stall of the centrifugal compressor. Frigne et al. [11] found that different types of vaneless diffusers caused differences in stall and the rotational velocity of the stall was related to the mass-flow rate. When the centrifugal compressor operates in design-deviating conditions, cavitation also contributes to the development of unstable flow structures. Ge et al. [12] discovered that the influence of temperature on the change in cavitation flow structure is explained by proper order decomposition analysis. Zhang et al. [13] further quantitatively analyzed cavitation volume expansion and structure development due to temperature rise. In additional, Ge et al. [14] proposed that the existence of cavitation will accelerate the development of incident flow and vortex structures. In the following decades, many researchers have devoted themselves to exploring the signs of stall precursors and preventing centrifugal compressors from entering stall conditions. The phenomenon of rotational stalling with tip clearance confirms that the boundary-layer separation produces low-energy fluid. Johnson et al. [15] thought that the separation of the boundary layer and the secondary flow are bound to generate pressure fluctuations. Greitzer et al. [16] proposed two typical stall precursors: the modal wave and spike wave. Modal waves appear as large-scale, long-wave disturbances. Moore et al. [17] believed that the number of modes was the number of stall clusters, another spike-type. The wave was a small-scale short-wave disturbance. These two stall precursors have been verified in low-speed axial compressors by Garnier et al. [18]. Spike-type stalls in centrifugal compressors were caught, and it was proposed that the spike signal in the rotating stall of the diffuser is caused by the back-flow vortex at the leading edge of the diffuser [19]. Pullan et al. [20] summarized much of the previous work and discussed in detail the formation mechanism of spikes in centrifugal compressors. The flow separation of the leading edge of the blade generated spike signals in the case of high-airflow angles. Mischoet et al. [21] described a signal that the blade resonance during stall can cause pressure fluctuations. Li et al. [22] proposed that, in the unsteady simulation, the pressure pulsation generated by the internal flow structure of the centrifugal pump will act on the diffuser. In general, the research on the unsteady flow of centrifugal compressors has lagged behind that of axial compressors. Day [23] predicted that many theorems regarding stall were more suitable for axial compressors. However, blade shape in centrifugal compressors is complex. The linear curvature and Coriolis force disturb the flow instability more severely, which leads to the differences between stall mechanisms in axial compressors. In general, most of the current research on centrifugal compressors focuses on rotating stall at low mass-flow rates. Meanwhile, where does the flow loss mainly occur in the key position of the centrifugal compressor at high mass-flow rates? How does flow separation in centrifugal compressors evolve in time and space at low flow rates (near-stall condition) and high flow rates? To optimize centrifugal compressors and to obtain a wide range of working conditions, the unsteady-flow characteristics of centrifugal compressors at the low (near-stall condition) and high flow rate conditions are worthy of our attention.

In this work, the main purpose is to analyze the pressure, velocity, and turbulent kinetic energy by the numerical simulation of a centrifugal compressor of a three-element impeller with tip clearance. The existing mechanism of boundary-layer separation and energy losses was studied under off-design conditions. The interaction was between the various components. The pressure and velocity fluctuations of unsteady flow were obtained in the centrifugal compressor by setting monitoring points. Joint analysis was used to explore the interaction and development mechanism of each component in the development of unsteady flow. This provides insight into widening the operating range and improving the operational safety of centrifugal compressors.

2. Governing Equations and Numerical Method

2.1. Governing Equations of Fluid Flow

No matter how complicated the turbulence is, unsteady continuity equations and Navier–Stokes (N-S) equations are still applicable to the instantaneous motion of centrifugal compressor flow.

The three-dimensional compressible continuity equation is

$$\frac{\partial \rho}{\partial t} + \nabla \cdot (\rho \mathbf{u}) = 0 \tag{1}$$

The momentum equation is

$$\frac{\partial (\rho \mathbf{u})}{\partial t} + \nabla (\rho \mathbf{u}\mathbf{u}) = -\nabla p + \nabla \cdot \tau + f \tag{2}$$

where ρ represents the fluid density,u is the macroscopic velocity of the mainstream, τ denotes the shear force, and f is the other external force, respectively.

The total energy equation used in the calculation is given as

$$\frac{\partial (\rho h_{tot})}{\partial t} - \frac{\partial p}{\partial t} + \nabla \cdot (\rho U h_{tot}) = \nabla \cdot (\lambda \nabla T) + \nabla \cdot (U \cdot \tau) + U \cdot S_M + S_E \tag{3}$$

where tot is the total enthalpy, which is related to the static enthalpy $h(T, p)$.

$$h_{tot} = h + \frac{1}{2} U^2 \tag{4}$$

2.2. K-ε Turbulence Model

The k-ε turbulence model is a widely used numerical simulation method. The turbulence model has strong adaptability and high resolution for the viscous layer and separation zone. Du et al. [24] compared k-ε with the shear stress transfer (SST), showing that the turbulent kineticenergy distribution at 50% blade height is almost the same. On the premise of ensuring calculation accuracy, k$-\varepsilon$ has a more economic effect. Standard k-ε model equations are given [25].

The turbulent kinetic energy equation k is

$$\frac{\partial (\rho k)}{\partial t} + \frac{\partial (\rho k u_i)}{\partial x_i} = \frac{\partial}{\partial x_j} \left[\left(\mu + \frac{\mu_i}{\sigma_k} \right) \frac{\partial k}{\partial x_j} \right] + G_k + G_b - \rho \varepsilon - Y_{\mathrm{m}} + S_k \tag{5}$$

The diffusion equation is

$$\frac{\partial (\rho \varepsilon)}{\partial t} + \frac{\partial (\rho \varepsilon \mu_i)}{\partial x_j} = \frac{\partial}{\partial x_j} \left[\left(\mu + \frac{\mu_i}{\sigma_\varepsilon} \right) \frac{\partial \varepsilon}{\partial x_j} \right] + G_{1\varepsilon} \frac{\varepsilon}{k} (G_k + G_{3\varepsilon} G_b) - C_{2\varepsilon} \rho \frac{\varepsilon^2}{k} + S_\varepsilon \tag{6}$$

where G_k denotes the turbulent kinetic energy derived from the velocity gradient in laminar flow, G_b is the turbulent kinetic energy derived from buoyancy, and Y_m is the fluctuation caused by excessive diffusion in compressible turbulent motion, respectively.

2.3. The Equation Introduction of LES

In general, the LES model has been implemented to simulate complex turbulence flow. Shahin et al. [26] confirmed that LES can predict flow characteristics under unsteady conditions. Small-scale fluctuation is filtered by the filtering function, and then large-scale fluctuation is simulated directly. Finally, small-scale fluctuation simulation is realized by the sub-grid scale. Smagorinsky et al. [27] originally proposed the LES calculation method in weather forecast research, and used the RANS model to propose the closed method of the LES equation. Yoshizawa proposed a Smagorinsky sub-lattice model suitable for compressible flow, and Speziable et al. [28] expanded the application range of the Smagorinsky sub-lattice model for compressible flow. Since then, LES Smagorinsky, as a widely used turbulence model, can describe small-scale turbulent flow with sufficient calculation accuracy and reduced calculation cost.

The k-ε model is used to simulate the steady-state of a centrifugal compressor on the premise of ensuring accuracy in the work. The steady-state calculation results are used as the initial conditions for unsteady calculations. The LES Smagorinsky sub-lattice model is used for unsteady calculations.

The N-s equation is processed by the filtering function to obtain the filtered turbulence control equation [27].

$$\frac{\partial \overline{u_i}}{\partial t} + \overline{u_j}\frac{\partial \overline{u_i}}{\partial x_j} = -\frac{1}{\rho}\frac{\partial p}{\partial x_i} + \nu\nabla^2\overline{u_i} - \frac{\partial \tau_{ij}}{\partial x_j} \tag{7}$$

where τ_{ij}=$\overline{u_i u_j} - \overline{u_i}\,\overline{u_j}$ refers to the sub-grid scale stress (SGS). The partial shear stress tensor is solved with $\overline{S_{ij}} = \frac{1}{2}\left(\frac{\partial \overline{u_i}}{\partial x_j} + \frac{\partial \overline{u_j}}{\partial x_i}\right)$.The mixing length hypothesis is used to solve the turbulent viscosity of SGS as $\mu_t = \rho(C_s\Delta)^2\sqrt{2\overline{s_{ij}}\,\overline{s_{ij}}}$. C_s is the Smagorinsky constant, and Δ denotes the filter size, respectively.

2.4. Geometry and Mesh Generation

The whole basin of the centrifugal compressor is used as the computational model (see Figure 1), including the inlet, outlet, impeller, vaneless diffuser, and volute. Table 1 shows the main geometrical parameters of the centrifugal compressor. The rotation rate of the centrifugal compressor is 10,545 rpm, and the designed mass-flow rate is 28.27 kg/s. The medium used inall numerical simulations is a new condensing agent R134a with a density of 4.25 kg/s in a gaseous state; a sort of heavy medium with complex physical and chemical properties. A gradually expanding inlet, outlet, and a three-dimensional flow impeller with good flow passage are adopted in the centrifugal compressor.

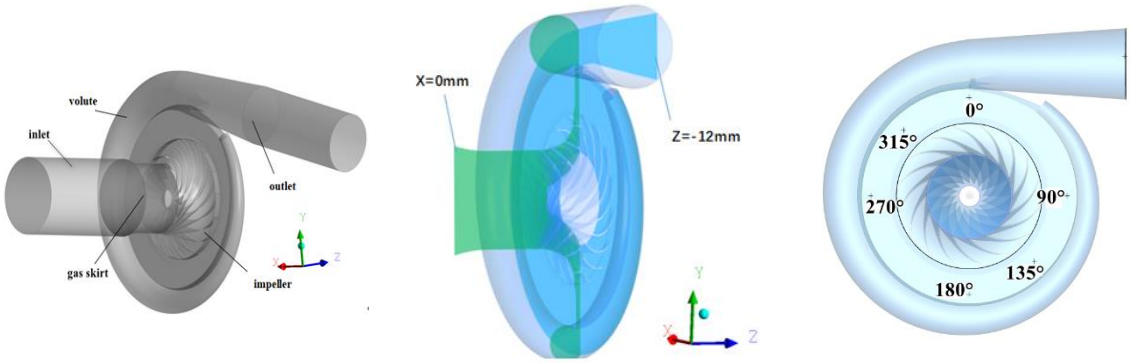

(**a**) (**b**) (**c**)

Figure 1. (**a**) Geometry of the centrifugal compressor; (**b**) Cross-sectional diagram showing the centrifugal compressor at x = 0 mm and z = −12 mm; (**c**) Description of orientations in the work.

Table 1. Main geometrical parameters of the centrifugal compressor.

Geometrical Parameters	Value
Inlet diameter (mm)	228
Outlet diameter (mm)	174
Impeller height (mm)	120
Width of impeller exit (mm)	25
Number of blades	16

Table 1 shows the geometric dimensions of the centrifugal compressor components. It should be noted that the impeller is composed of 16 three-dimensional blades, the design incidence angle of the blade is 145°, and the outlet angle is 90°, respectively.

The computational domain grid of the fluid is based on ANSYS ICEM. Figure 2 shows the structured grid generated by O-block and Y-block division. The blade tip and volute tongue are grid-encrypted.5021974grid nodes are implemented in the numerical simulations, and the number of grids is 4,794,000. The overall grid quality, aspect ratio, and maximum corner meet the requirements of accurate calculations. Figure 2c shows the distribution of y-plus values near the blades and impeller hub. In this paper, the global structured grid is used for calculation. As the rotating structure, the grid is refined for the blades. According to the results of steady calculation under design conditions, the grid satisfies the limitation of y-plus within 30 for the Large Eddy Simulation turbulence model.

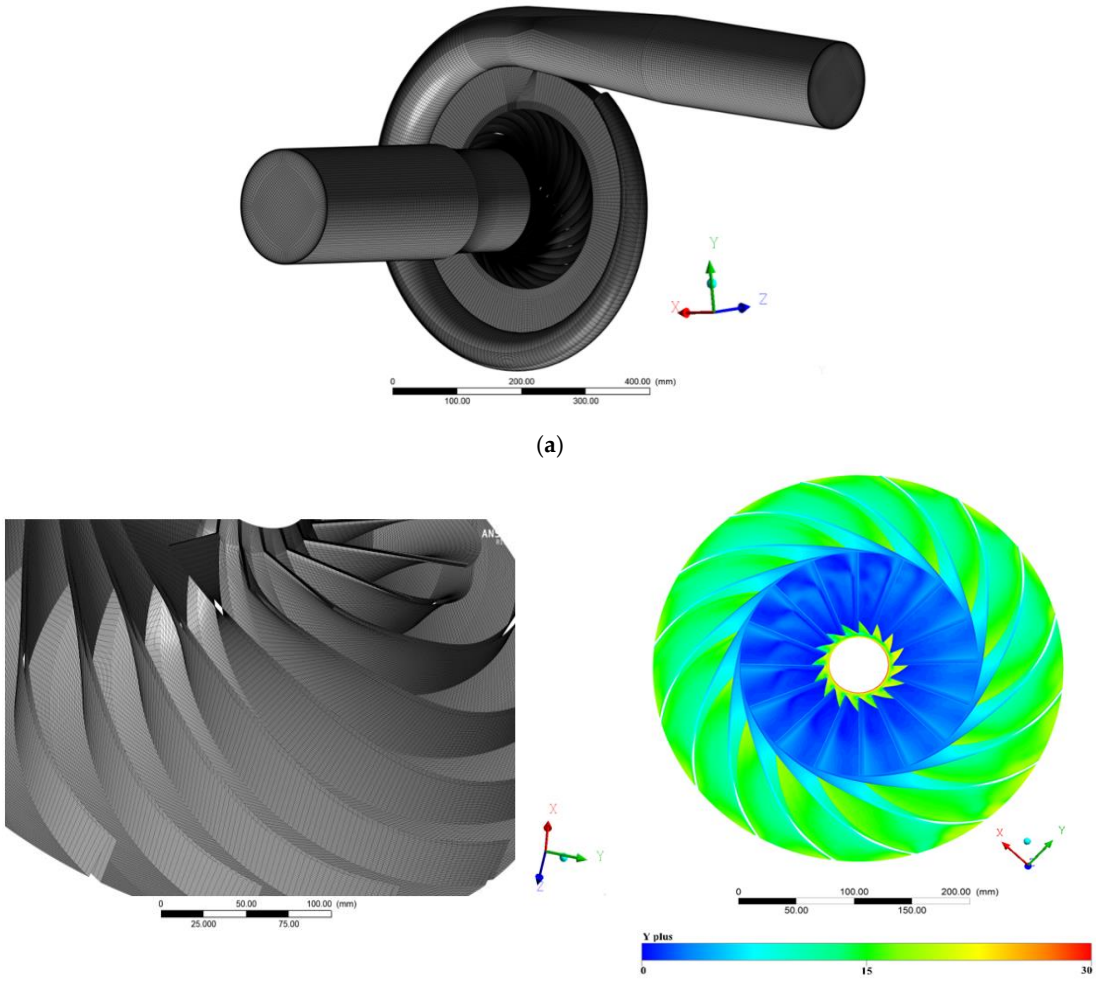

Figure 2. Overall grid division diagram of centrifugal compressor. (**a**) Grid of centrifugal compressor. (**b**) Grid of the impeller. (**c**) Distribution of y-plus values near the blades and impeller hub.

Figure 3 displays the total pressure ratio and efficiency characteristic curves of the centrifugal compressor. The blue line denotes the total pressure ratios of the centrifugal compressor, and the red line represents the isentropic efficiency of the centrifugal compressor. As shown in Figure 3, the total pressure ratio of the centrifugal compressor decreases with an increase in the mass-flow rate when the flow rate is higher than 23 kg/s. The highest efficiency point is 28.27 kg/s (Qn),the designed operating condition. The pressure ratio drops when the flow rate is lower than 23 kg/s. The 23 kg/s flow rate is near the stall point of the centrifugal compressor.Aflow rate of 22.62 kg/s (0.8 Qn) is regarded as the near-stall condition. Thus, a flow rate of 22.62 kg/s (0.8 Qn) is implemented to study the spatiotemporal evolution and fluctuation characteristics of the centrifugal compressor in this paper.

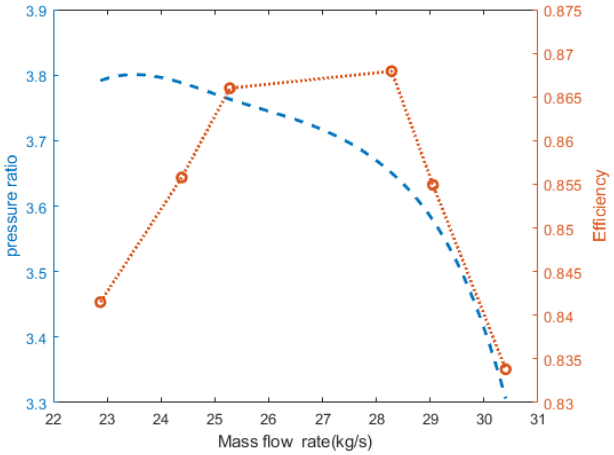

Figure 3. Pressure ratio and efficiency characteristic curves of the centrifugal compressor.

2.5. Boundary Condition

In general, the ANSYS CFX is implemented to simulate the centrifugal compressor. In the boundary condition of CFX, the mass-flow rate is used in the inlet of the centrifugal compressor, and static pressure is implemented at the outlet of the centrifugal compressor. The four cases' corresponding numerical relationship are shown in Table 2. The total pressure is adopted at inlet; its value is 360 kPa, and the total temperature at inlet is set to 278.15 k.

Table 2. Correspondence of flow and outlet static pressure.

Case	Q (kg/s)	Pout(kPa)
I	30.56	800
II	28.27	927
III	25.48	977
IV	22.62	995

3. Numerical Results and Discussions

3.1. Circumferential and Axial Analysis of the Steady Velocity and Pressure Fields

Figure 1b shows the location of the section in Figure 4. The internal flow characteristics of the centrifugal compressor are analyzed from the axial x = 0 section based on the velocity streamline. At the high mass-flow condition (1.1 Qn = 30.56 kg/s), a distinct low-velocity region mainly occurs near the vaneless diffuser and tongue as illustrated in Figure 4a. The streamline deviates from the arc of the wall in the volute and strikes the inner wall of the volute, causing a lot of impact losses. Compared with small mass-flow rates, the velocity of the impeller is obviously higher than that of other regions and the velocity of the vaneless diffuser is obviously lower than that of other regions.

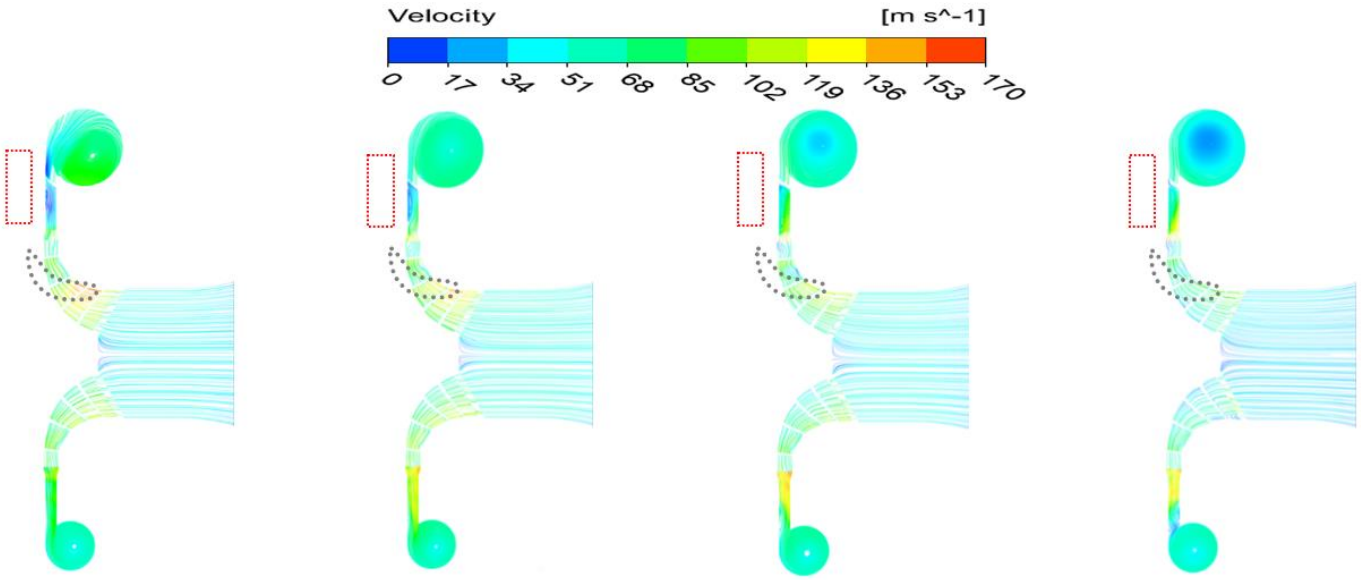

(**a**) 30.56 kg/s (**b**) 28.27 kg/s (**c**) 25.48 kg/s (**d**) 22.62 kg/s

Figure 4. Streamline for different mass-flow rates in x = 0mm section.

Figure 4b exhibits the velocity stream line of the x = 0 mm section of a centrifugal compressor under the designed conditions (Qn = 28.27 kg/s). The streamline of the centrifugal compressor is very smooth in the designed conditions. Figure 4c shows the velocity stream line of the x = 0 mm section of a centrifugal compressor inthe low mass-flow rate case of 0.9 Qn = 25.48 kg/s. It is clearly seen that a little separated flow appears at the suction surface of the impeller. The streamline at the blade tip gap is chaotic, and the incident angle of the fluid is inconsistent with the blade design angle, which reduces mainstream energy. The fluid is aggravated by viscous force, and boundary-layer separation occurs, which is confirmed by the lower impeller speed. At the junction of the impeller and the vaneless diffuser, large velocity gradients are exhibited, and the fluid mixing losses increase, which inevitably leads to acomplexity of flow in the vaneless diffuser. The axial cross-sectional schematic diagram shows that eddies exist in the vaneless diffuser, and the velocity is significantly lower than that of the design conditions in the volute.

Figure 4d plots the velocity streamline of the x = 0 mm section of a centrifugal compressor in the lower mass-flow rate case of 0.8 Qn = 22.62 kg/s (near-stall condition). It is clearly observed that with the decrease in mass-flow rate, flow separation occurs on the blade pressure surfaceof the impeller, and back-flow is even observed at the inlet of the impeller. Moreover, the flow instability is more serious in the vaneless diffuser, and the low-speed area becomes increasingly wide in the volute. To sum up, the blade tip clearance is a sensitive zone for unstable flow. If the mass-flow rate deviates from design conditions, the airflow angle will not match the blade design angle, which enhances the energy loss of the mainstream and causes flow instability inside the centrifugal compressor.

Figure 5 displays the distribution of the velocity and streamline in the Z = −12 mm section at different mass-flow rates.

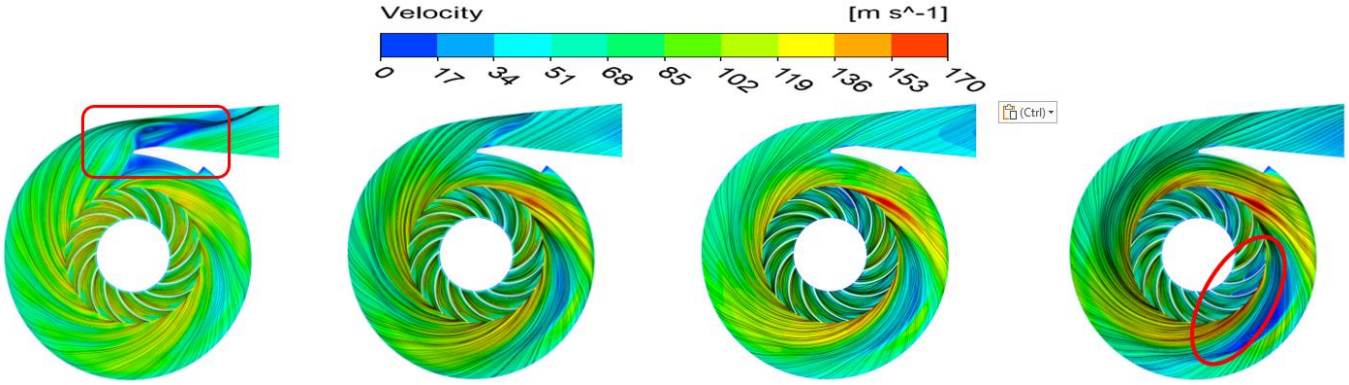

(**a**) 30.56 kg/s (**b**) 28.27 kg/s (**c**) 25.48 kg/s (**d**) 22.62 kg/s

Figure 5. Distribution of the velocity and streamline in the Z = −12mm section at different mass-flow rates.

Figure 5a shows the distribution of the velocity and streamline at the Z = −12 mm section and the high mass-flow rate (1.1 Qn = 30.56 kg/s). The high mass-flow rate represents excessive velocity in the impeller. Slight flow separation occurs at the end of the blade channels with the streamlines converging towards the pressure surface. Terrible velocity gradients are observed at the junction of the impeller outlet and the vaneless diffuser, which results in considerable mixing losses. The low-speed zones and eddies near the volute tongue are noted as causing blockage of the centrifugal compressor. The presence of vortices indicates that the fluid needs to overcome a large negative pressure gradient to work, which is not conducive to the development of turbulence. Figure 5b shows the distribution of the velocity and streamline at the Z = −12 mm section in the design condition (Qn = 28.28 kg/s). The streamline of the volute and impeller is smooth and the permeability of blade passage is excellent. At the same time, the vaneless diffuser shows the positive effects of speed reduction and pressurization.

Figure 5c displays the streamline distribution with velocity contour as background at the Z = −12 mm section in the 25.48 kg/s condition (0.9 Qn). The overall velocity in the impeller decreases and secondary flow occurs in the two flow channels located at 0°. At a low mass-flow rate, flow separation occurs preferentially in one or several channels, which is confirmed by Dodds [7]. The upper instability of the vaneless diffuser under centrifugal force was produced by the low-speed fluid at the impeller outlet.

Figure 5d exhibits the distribution of the velocity and streamline at the Z = −12 mm section at the lower mass-flow rate of 0.8 Qn = 22.62 kg/s (near-stall condition). When the mass-flow rate is further reduced, the density of streamlines changes at 60° and 210°, which is caused by the non-uniformity of the velocity gradient. This phenomenon develops from the outlet of the impeller to the vaneless diffuser. Additionally, slow flow is observed in more blade channels. The airflow angle changes at low mass-flow rates, while the back-flow of the tip clearance reduces the energy of the main flow, resulting in a more pronounced effect of viscous force and more severe boundary-layer separation. Furthermore, as the mass-flow rate decreases, the stall extent and area of the vaneless diffuser are further expanded, and large-scale, low-speed vortices exist, causing more mixing losses. Flow instability is exacerbated downstream of the vaneless diffuser, which is consistent with the work by Elias et al. [29].

Our research reveals the stall mechanism in two different off-design conditions. For high mass-flow rate conditions, high-speed fluid impacts the volute tongue, resulting in a large amount of impact loss eddies beingformed at the volute tongue, which causes the blockage of the centrifugal compressor. As for low mass-flow rate conditions, the flow separation at the trailing edge of the blade is caused by the backflow at the tip clearance As the mass-flow rate decreases, flow separation intensifies, which gives rise to the main flow energy becoming too low.

Figure 6a–d show the contours corresponding to the static pressure value of four different mass-flow rates at the z = −12 mm section. Figure 1b presents the cross-section.

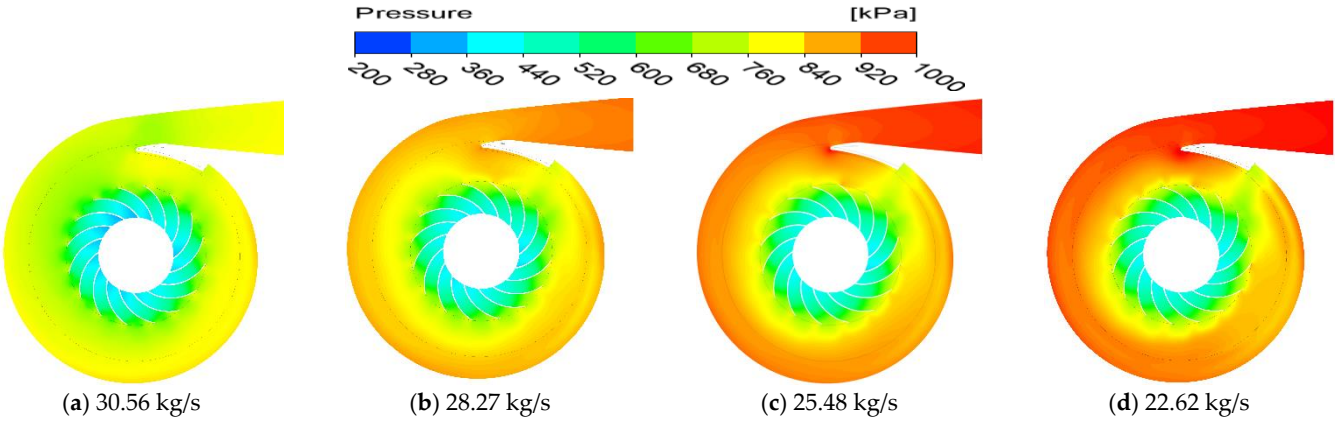

(**a**) 30.56 kg/s (**b**) 28.27 kg/s (**c**) 25.48 kg/s (**d**) 22.62 kg/s

Figure 6. Contours corresponding to a static pressure value illustrated in Figure 6a–din the Z = −12 mm section at different mass-flow rates.

Figure 6a exhibits the static pressure contour of the high mass-flow rate(30.56 kg/s). A considerable radial static pressure gradient mainly appears in the impeller. Compared with the low mass-flow rates, the case of 1.1 Qn = 30.56 kg/s shows globally low pressure and a slight static pressure gradient across the vaneless diffuser and volute.

Figure 6b shows the static pressure distribution under the design conditions (Qn = 28.27 kg/s). Naturally, the unique diverging runners of the centrifugal compressor produce a superb deceleration and supercharging effect. Furthermore, the pressure gradient of the vaneless diffuser and the volute is stable.

Figure 6c shows the static pressure contour at mass-flow rate of 0.9 Qn = 25.48 kg/s. It is clearly seen that the vaneless diffuser and volute exhibit a higher static pressure area; the radial static pressure gradient of the vaneless diffuser and volute are larger than the design condition. However, there is no such obvious phenomenon in the impeller. A zone of high pressure is observed at the volute tongue, which is a sensitive zone for pressure fluctuations. We found a low-pressure region appearing at 45°; it can be related to the jet-wake structure. Unstable flow is frequently found in vaneless diffusers, as previously shown by Hellstrom et al. [30]. They argued that the low-speed area in the vaneless diffuser and volute is mainly caused by a large pressure gradient.

Figure 6d exhibits the static pressure distribution at near-stall conditions (0.8 Qn = 22.62 kg/s). As shown in Figure 6d, one can see that the radial pressure gradient of the vaneless diffuser and volute obviously enhance with a decrease in the mass-flow rate. A dramatic pressure gradient appears circumferential of the diffuser under unsteady flow, as explained by Liu et al. [31].

At a high mass-flow rate, more energy exists in the form of kinetic energy, which is why the static pressure of the centrifugal compressor is lower than that of the design conditions. The static pressure gradient is almost slight, while the radial static pressure gradient is enhanced in the vaneless diffuser and volute. Nevertheless, the influence of the pressure gradient in the impeller is milder, which is confirmed by Semlitsch et al. [32]. For low mass-flow rates, the static pressure value is greater than that of the design conditions, which is a symbol of low-speed flow. In addition, the excessive static pressure gradient appears at the vaneless diffuser of centrifugal compressor, and the work required to overcome the adverse pressure gradient is unreasonable.

Figure 7 represents the distribution of turbulent kinetic energy at 50% blade height at four different mass-flow rates. Figure 7a shows the distribution of turbulent kinetic energy at the high mass-flow rate (1.1 Qn = 30.56 kg/s). It is obvious that a large amount of TKE is generated at the blade's outer diameter at the high mass-flow rate (1.1 Qn = 30.56 kg/s). Turbulent kinetic energy exists for overcoming large energy dissipation to continue the development of turbulence, which cause kinetic energy loss of the mainstream. As shown

in Figure 6a, the massive energy is lost due to the excessive back-pressure gradient at the impeller outlet.

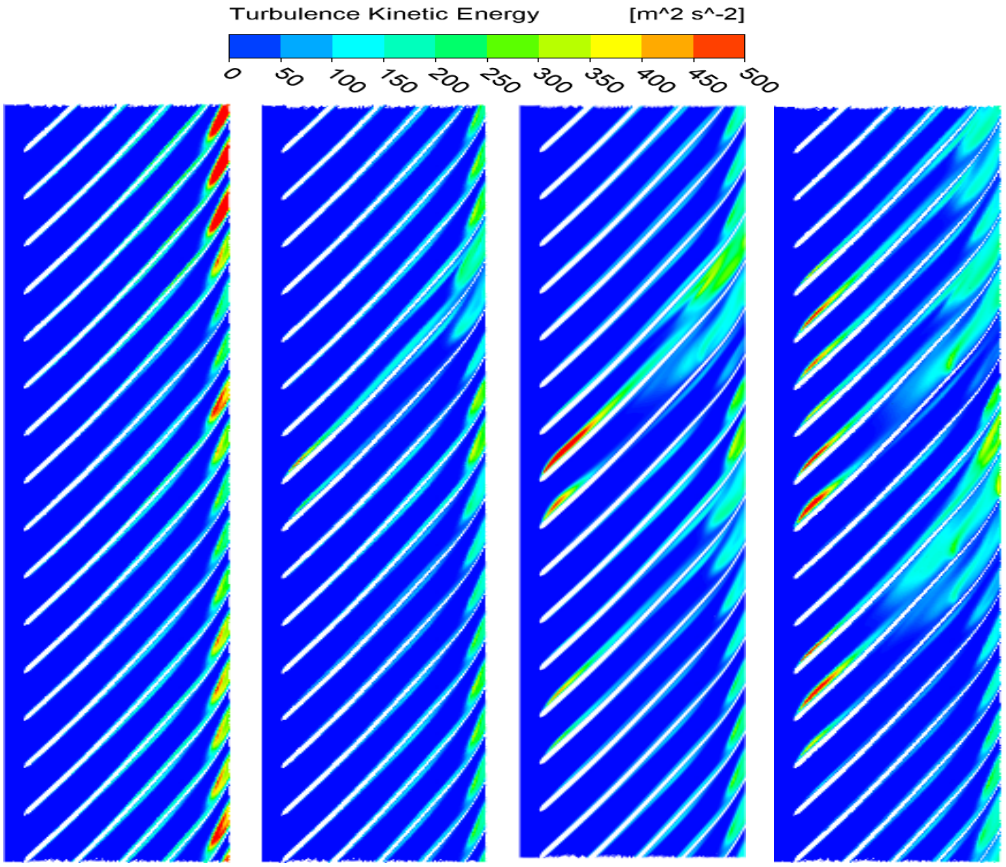

(**a**) 30.56 kg/s (**b**) 28.27 kg/s (**c**) 25.48 kg/s (**d**) 22.62 kg/s

Figure 7. Comparison of turbulent kinetic energy at 50% blade height under four different mass-flow rates.

Figure 7b shows that the status of turbulent kinetic energy underthe design conditions (28.27 kg/s). When the mass-flow rate reduces to 25.48 kg/s (see Figure 6c), TKE is generated on the suction surface of several flow runners due to the flow separation. The development of turbulence is maintained by the resulting TKE in poor flow channels. Flow channels that generate TKE are often identified as appearing with flow separation, which is an unfavorable phenomenon coming at the expense of mainstream energy.

Figure 7d displays the statistic of turbulent kinetic energy at the lowest mass-flow rate (0.8 Qn = near-stall condition). It can be noted that more channels produce TKE with decreased mass-flow rates. In general, the presence of the TKE is an adverse phenomenon for the efficiency of the centrifugal compressor. Excessive TKE production means clogged centrifugal compressors at the high/low mass-flow rates. From the analysis of Figure 6, the work provides an insight into the flow instability of impellers under different off-design conditions. The high flow losses in the impeller mainly occur in different suction surfaces of the blade passage at high and low mass-flow rates.

3.2. Unsteady Analysis of Internal Flow in the Centrifugal Compressor

For unsteady computational data acquisition, the time-step size is set to 3.16×10^{-5} s in this paper. We obtain a set of data for every two degrees of rotation. The unsteady numerical results of the centrifugal compressor after 10 revolutions are adopted to ensure the accuracy of the numerical simulation. Figure 8 shows the development of the velocity field and the distribution of streamlines at the z = −12 mm cross-section and the high mass-flow rate (1.1 Qn = 30.56 kg/s). The characteristic of the high mass-flow rate is

blockage; as shown the red elliptical area in the Figure 8, the velocity contours present the low-velocity areas and eddies near the volute tongue. From Figure 8a–c, we can clearly see the development process of the eddies at the tongue, which is decomposed into two small eddies from a large eddy. The separation of the vortex is more conducive to the circulation of the centrifugal compressor. As the separation of the vortex progresses, the low-speed blocking area at the outer ring of the volute tongue disappears and the low-energy fluid is discharged from the outlet of the volute, as can be observed in Figure 8c. This provides insight into turbulent energy transfer. The large eddies cause serious destruction of the average mainstream, the existence of eddies inevitably leading to a sudden change in the pressure gradient where a large amount of the energy conversion takes place. The mechanism of the small eddy is mainly to convert the energy of the large eddy into heat and dissipate it. Moreover, the large eddy current exhibits anisotropy with certain stagnation characteristics, while the isotropic performance of the small eddy current is indicated. These small vortices are better able to drain the compressor with the mainstream. Compared with the design conditions, a larger flow velocity in the impeller can be noted with a high mass-flow rate. The flow separation in the blade channel is mainly manifested in the outer diameter of the blade. Serious boundary-layer separation is observed at the suction surface of the trailing edge of the blade, resulting in a jet structure. Under the action of centrifugal force and Coriolis force, bundled streamlines are observed and the streamlines show inferior conformability with the inner wall of the volute.

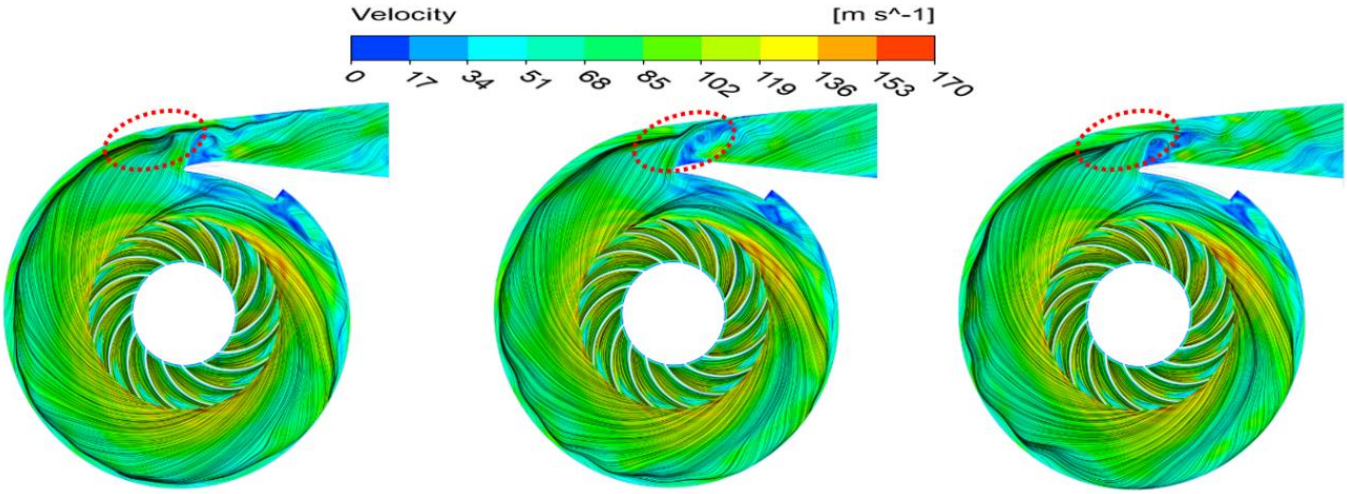

(**a**) t + 1/3T (**b**) t + 2/3T (**c**) t + T

Figure 8. Development of the velocity and streamline at the z = −12 mm cross-section and the high mass-flow rate(1.1 Qn 30.56 kg/s) from 0.0569 to 0.06259 s.

Figure 9 exhibits the velocity field situation and streamline distribution at the z = −12 mm cross-section and the near-stall mass-flow rate (0.8 Qn = 22.62 kg/s). In general, acomplexity of internal flow is observed at a low mass-flow rate. The extreme inhomogeneity of the velocity field brings about an excessive velocity gradient. At a constant speed of 10,545 rpm, centrifugal and Coriolis forces intensify the effect on low-energy flow in the impeller, accompanied by the squeezing of high-speed groups in the vaneless diffuser—which reveals that most streamlines are distributed in bundles.

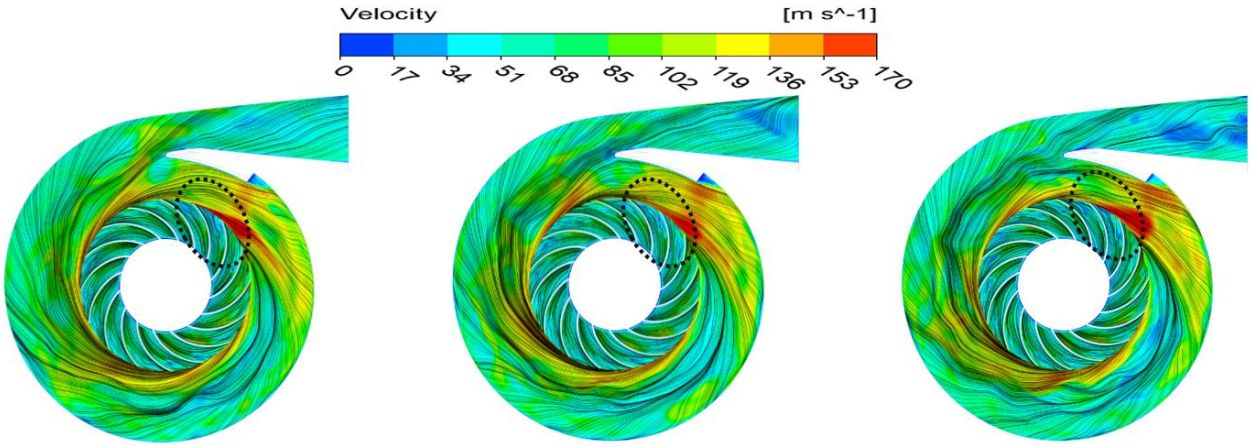

(**a**) t + 1/3T (**b**) t + 2/3T (**c**) t + T

Figure 9. Development of the velocity andstreamlineat z = −12 mm cross-sectionand the near-stall mass-flow rate (0.8 Qn = 22.62 kg/s) from 0.0569 to 0.06259 s.

Figure 10 shows the distribution and development of pressures at the z = −12 mm cross-section and near-stall mass-flow rate (0.8 Qn = 22.62 kg/s). A widely low-pressure zone at 45° is seen and the appearance of the lowpressure leads to excessive energy exchange. With time evolution, the low-pressure zone gradually increases. From Figure 10a–c, the high-pressure region at the vortex tongue gradually expands, resulting in a greater squeeze of the downstream fluid on the main flow. In addition, almost all blade channels in the impeller present low-speed zones and flow separation, which is caused by the stratification of the suction-surface boundary layer due to the low mainstream energy.

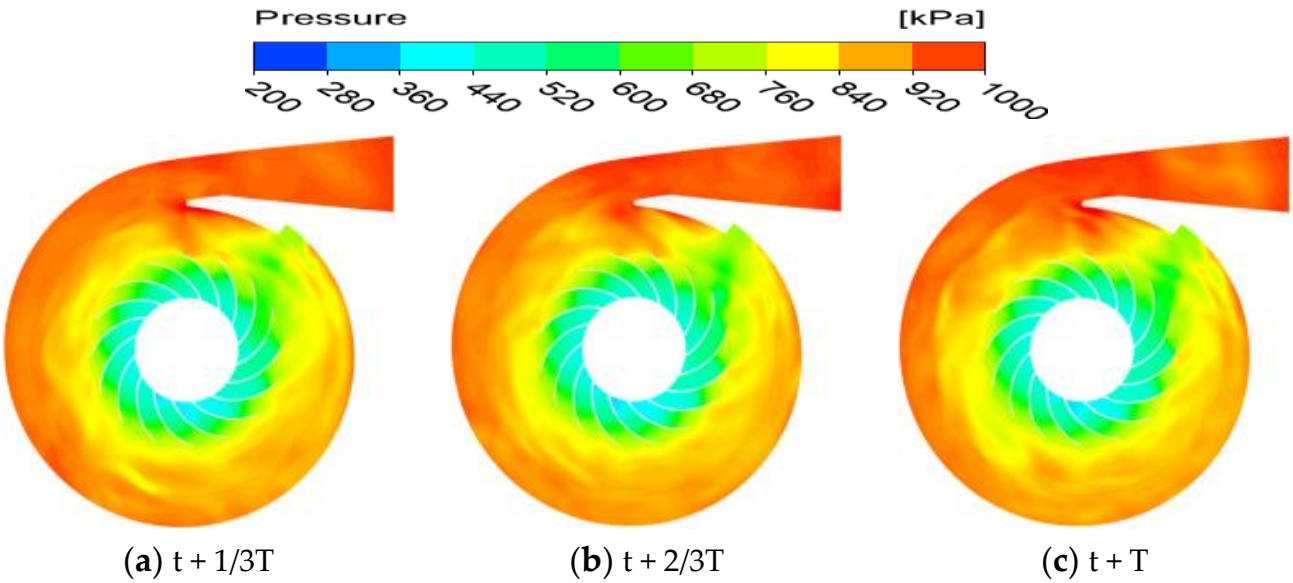

(**a**) t + 1/3T (**b**) t + 2/3T (**c**) t + T

Figure 10. Distribution and development of pressures at the z = −12 mm cross-section and near-stall mass-flow rate (0.8 Qn =22.62 kg/s) from 0.0569 to 0.06259 s.

From Figure 9a–c, one can see that the fluid is deflected circumferentially and the flow instability within the impeller is exacerbated, which is a precursor to the appearance of secondary flow. Overtime, flow deterioration is observed at 120° of the vaneless diffusers and at the volute outlet. Abrupt changes occur in the velocity gradient, resulting in more energy losses and lower efficiency than that of design conditions.

Figure 11 describes how three points are selected in a flow channel at 30%, 50%, and 90% blade height. Figure 12 shows the velocity fluctuation of three detection points located

at different axial heights (30%bh, 50%bh, 90%bh) in a blade channel, and the straight line is the average value of the fluctuation. According to the unsteady calculation, the temporal and spatial variation of the internal flow in the centrifugal compressor impeller is analyzed to provide some flow characteristics under off-design conditions.

Figure 11. Monitoring points in the channel.

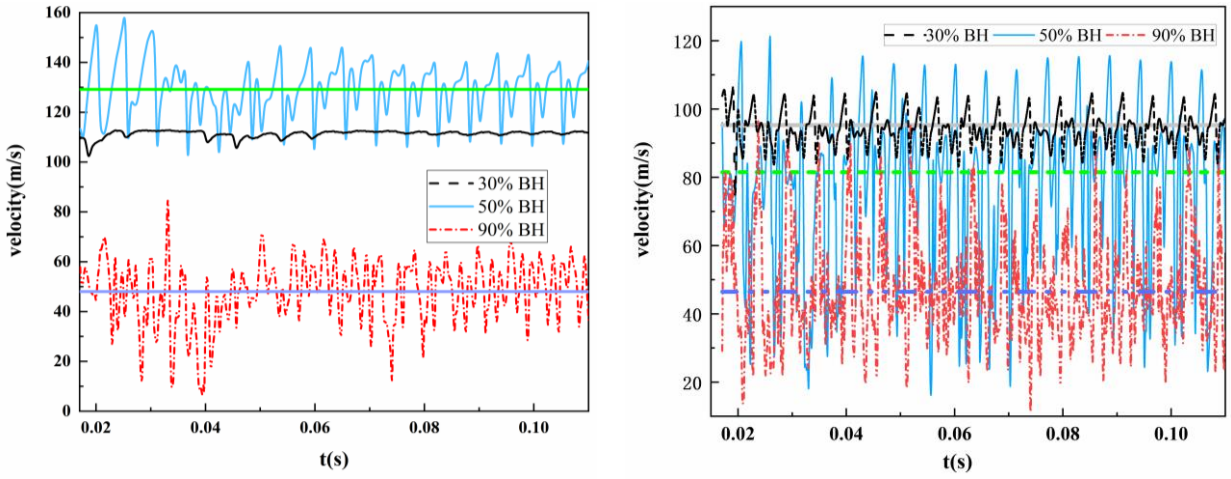

(**a**) 30.46 kg/s (**b**) 22.62 kg/s

Figure 12. Velocity fluctuation analysis of monitoring points at 30%, 50%, and 90% of the blade height in a certain blade channel under non-design conditions.

Figure 12a exhibits the velocity fluctuations of different blade heights (30%bh, 50%bh, and 90%bh) under the high mass-flow rate conditions (1.1 Qn = 30.46 kg/s). Velocity fluctuation is not violent at 30% blade height, and the flow is relatively stable in the tip clearance, indicating that small impacts are caused by the internal-flow instability of the tip clearance at the high mass-flow rate. The velocity fluctuation of the monitoring point at 50% and 90% of the blade height is very strong, which is caused by the velocity field disturbance in the boundary-layer separation of the impeller suction surface. Furthermore, the velocity fluctuation at 50% blade height is obviously higher than that of 90% blade height. This is mainly due to the self-regulating ability of the expanding channel of the centrifugal compressor. Flow instability mainly occurs in impellers and vaneless diffusers, which is well-consistent with that studied by Lou et al. [33]. The locations of these starting points of flow disorder are refined in the work. In general, the boundary layer separation of impeller suction surface appears at 30-to-50% blade height at a high mass-flow rate. The flow instability characteristics at 50% blade height are more serious than those at 90% due to the narrow diameter. Figure 12b shows the velocity fluctuation of different blade heights (30%bh, 50%bh, and 90%bh) at the near-stall mass-flow rate(0.8 Qn = 22.62 kg/s). Compared with 50% blade height, the fluctuation of the monitoring points at 90% blade height becomes moderate, indicating that the starting point of the velocity disturbance is at 30–50% blade height. The velocity fluctuates drastically at the monitoring points of 50% blade height. In the same near-stall mass-flow rate case (0.8 Qn = 22.62 kg/s), the fluctuation of the trailing edge of the blade at 90% blade height is more stable than that at 50%blade

height. By comparing velocity fluctuations, the fluctuation amplitude of the impeller at the near-stall mass-flow rate is more apparentthan that at the high mass-flow rate (30.46 kg/s). Flow separation occurs earlier at the near-stall mass-flow rate when comparing the velocity fluctuation of 30% blade height in Figure 12a,b. At 50% blade height, the average flow velocity forthe high mass-flow rate is much larger than that ofthe near-stall mass-flow rate, indicating that more serious diversion losses and lower mainstream energy appear under near-stall conditions (0.8 Qn = 22.62 kg/s).

Fast Fourier transform (FFT) is implemented to analyze unsteady flow in rotating machineries, which can provide some insights to understanding the internal flow by transforming the time domain into the frequency domain. Figure 13 plots the amplitude spectra obtained by FFT for pressure fluctuations at points A1, A2, and A3 at different mass-flow rates. Figure 13a exhibits the amplitude spectra of monitors at the high mass-flow rate (30.46 kg/s). The pulsation at 50% and 90% of the blade height is dominated by frequency conversion. However, high amplitudes occur at90% of the blade height of the impeller outlet. Figure 13b shows the amplitude spectra of monitors at near-stall conditions (0.8 Qn = 22.62 kg/s). The pulsation at 30%, 50%, and 90% of the blade height is dominated by frequency conversion. The rotational stall frequency and frequency multiplication show a difference in off-design conditions. The amplitude of pointA2 (50% BH) is lower than that of pointA3 (90% BH) at the same mass-flow rate, but the number of characteristic frequencies at point A2 is more than that at point A3. In general, the stronger instability occurs in the impeller of the centrifugal compressor at near-stall conditions (0.8 Qn = 22.62 kg/s).

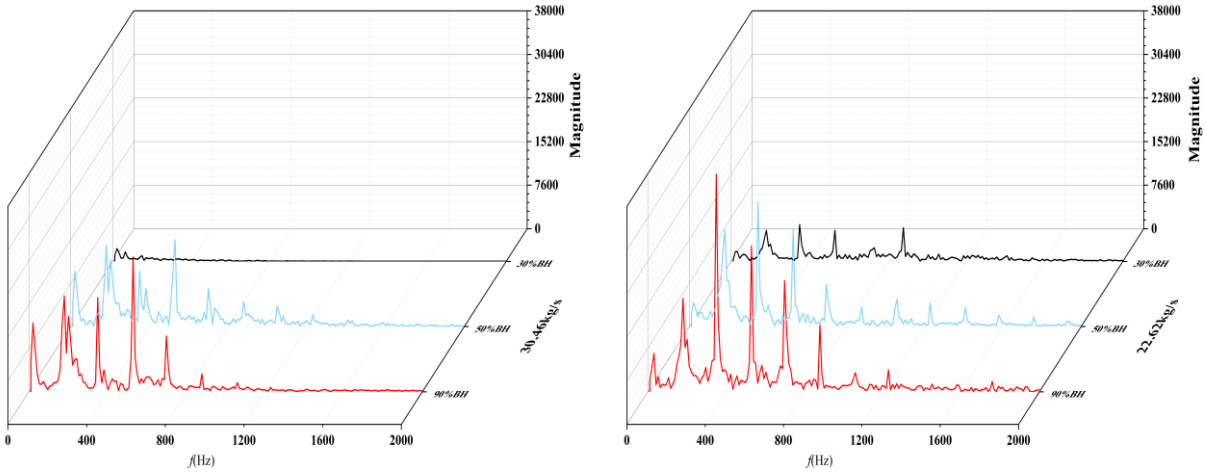

(**a**) 30.46 kg/s (**b**) 22.62 kg/s

Figure 13. Amplitude spectra of monitoring point at different blade heights (30%,50%,90%) in off-design conditions.

Figure 14 displays the amplitude spectra of monitoring point A3 under the two off-design conditions. In Figure 14a,b, the amplitude of point A3 at the impeller outlet is analyzed. The stall frequency is calculated to obtain a high mass-flow rate of 21.2 Hz, while the near-stall mass-flow rate is 31.8 Hz. The frequency spectrum of the impeller outlet at the high mass-flow rate (30.46 kg/s) is calculated in Figure 14a. It is obtained that the first, second, and third characteristic frequencies are 3.014 fn, 1.025 fn, and 1.989 fn, respectively. As shown in Figure 14b, the frequency spectrum of the impeller outlet at 20.62 kg/s (near-stall) is analyzed, and its characteristic frequencies are 1.989 fn, 3.014 fn, and 3.979 fn, respectively. These characteristic frequencies may be related to boundary-layer separation in the blade channels and the jet at the impeller outlet. Comparing to the two different mass-flow rate conditions, there is a characteristic frequency with a prominent amplitude at the near-stall mass-flow rate.

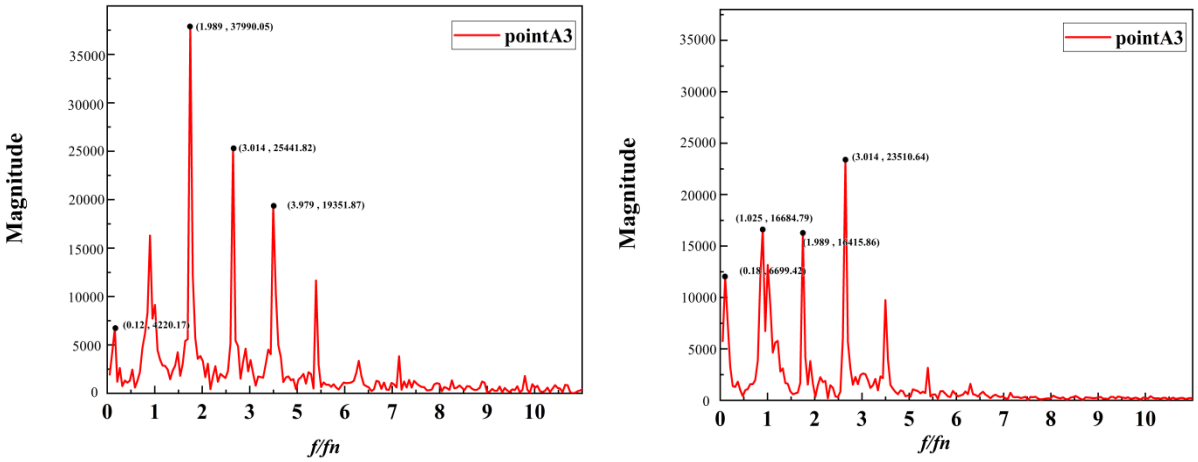

(**a**) 30.46 kg/s (**b**) 22.62 kg/s

Figure 14. Amplitude spectra of monitoring point A3 underthe off-design conditions.

Figure 15a shows the velocity fluctuations at the monitoring points of the tongue and the four calculation cases. Compared with the design conditions (28.27 kg/s), the velocity fluctuation is clearly lower near the tongue at the high mass-flow rate. Moreover, several amplitudes deviating from the mean value are observed, which is closely related to low-velocity eddies at the tongue (see Figure 8). At the near-stall mass-flow rate, periodic high-amplitude fluctuations are exhibited at the tongue, which aggravates with decreased flow. Figure 15b shows the velocity fluctuation at monitoring points of the outlet. It is further found thata sudden, irregular velocity fluctuation appears in the outlet of the centrifugal compressor at all off-design conditions, but the peak value of the fluctuation gradually increases with the distance from the design working point, which quantitatively reveals that the stall cell is gradually increasing at the cochlear tongue and exit sites of the centrifugal compressor, and the intensity of the stall cell blockage is also enhanced with decrease inflow rate. Figure 15 further verifies that blockage occurs near the outlet and the internal worm tongue of the compressor with decreasing flow rate in Figure 5.

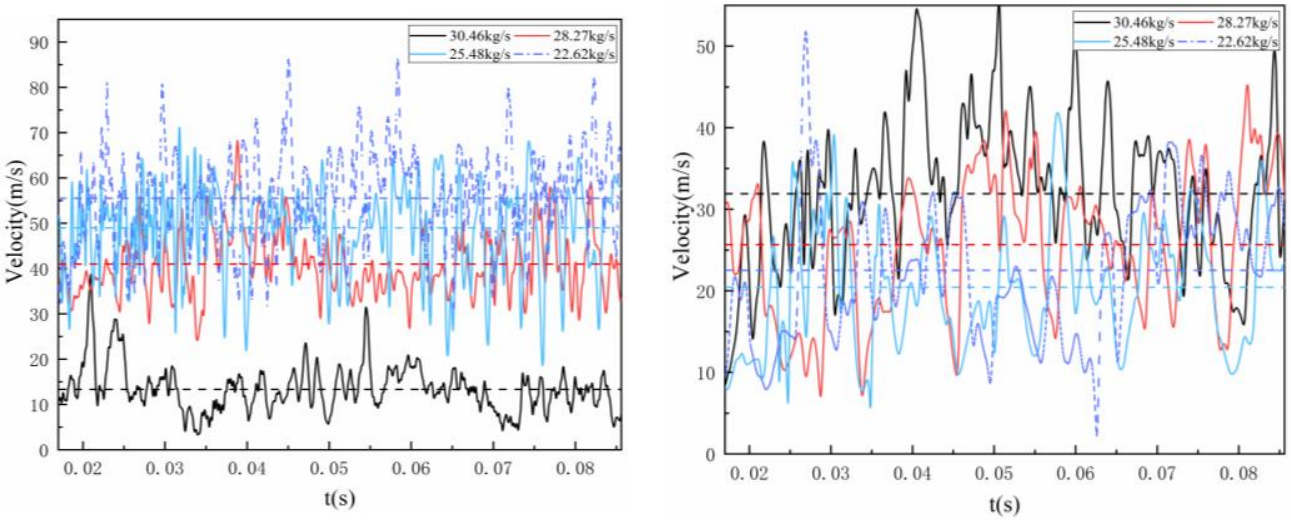

(**a**) tongue (**b**) outlet

Figure 15. Velocity fluctuation at monitoring points of tongue and outlet and four different mass-flow cases.

Figure 16 shows the pressure fluctuations at the monitoring points of tongue and outlet at different mass-flow rates. The same pressure-fluctuation trend is found at the tongue

and outlet. However, the change influctuation frequency at the tongue is greater than that at the outlet. At the high mass-flow rate, the pressure fluctuation at the volute tongue and outlet is more intense than that at the near-stall mass-flow rate (0.8 Qn = 22.62 kg/s). The fluctuation of pressure is more intense and many spike signals appear at the near-stall mass-flow rate when compared with the design condition (Qn = 28.27 Kg/s). The unstable flow complexity of the centrifugal compressor volute is demonstratedunder off-design conditions. Pressure fluctuations at the volute deteriorate the flow field, which is well-consistent with the previous work by Guo et al. [34].

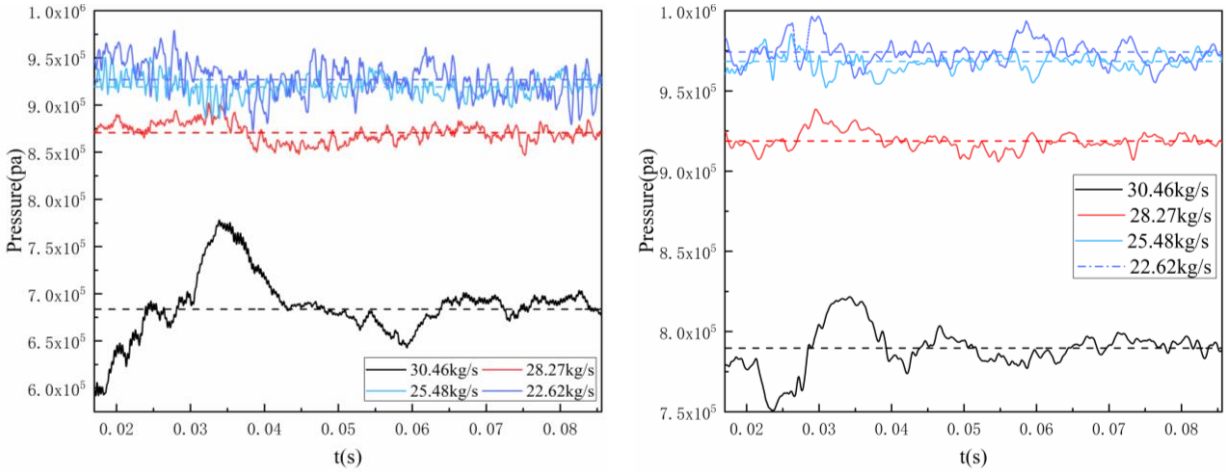

(**a**) tongue (**b**) outlet

Figure 16. Pressure fluctuation at monitoring points of the tongue and outlet at four different mass-flow rates.

Figure 17 shows the schematic diagram of the monitoring points on the vaneless diffuser. The data of these monitoring points are collected to analyze the spectrum of circumferential pressure fluctuations on the vaneless diffuser by FFT.

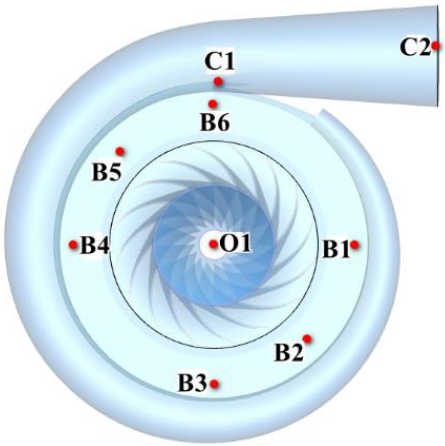

Figure 17. Monitoring points in the vaneless diffuser.

Figure 18 displays the amplitude spectrum of monitoring points of the vaneless diffuser for one circumferential turn at two different mass-flow rates. Figure 18a illustrates the amplitude spectrum at the high mass-flow rate (1.1 Qn = 30.46 kg/s). Illustrated in Figure 18a, it is noted that the pressure fluctuation period in the vaneless diffuser is mainly dominated by the blade passing frequency and its frequency multiplication. Meanwhile, the rotating stall frequency is almost negligible.

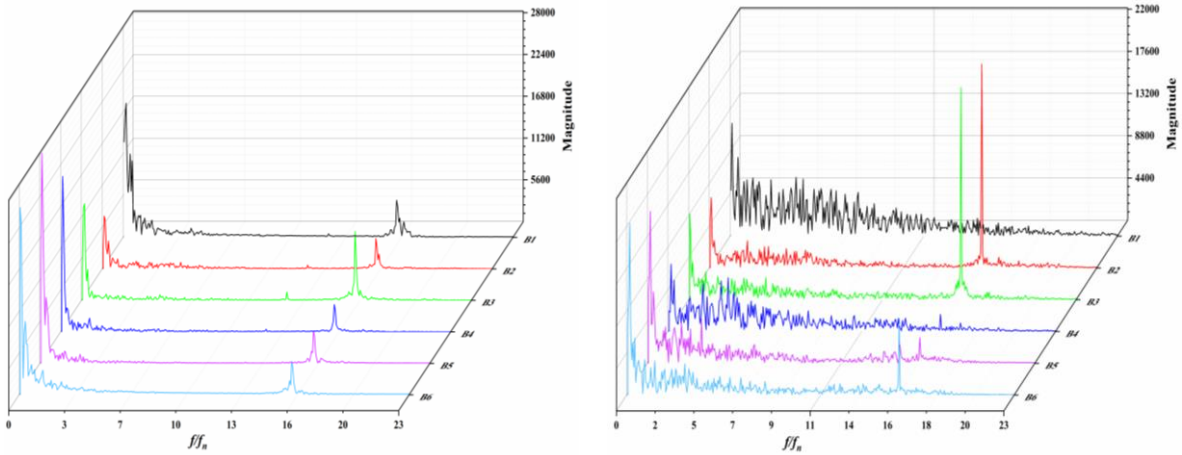

(**a**) 30.46 kg/s (**b**) 22.62 kg/s

Figure 18. Amplitude spectrum of monitoring points in the vaneless diffuser.

Figure 18b shows the spectral analysis of monitoring points regarding pressure fluctuations of the vaneless diffusers at the near-stall mass-flow rate, including blade passing frequencies and theirfrequency multiplication. Meanwhile, numerous low-frequency fluctuations are observed in the vaneless diffusers of the centrifugal compressor. The amplitude value of the blade frequency at different locations is distinguished at the near-stall mass-flow rate (0.8 Qn = 22.62 kg/s), which is related to the jet-wake structure in the vaneless diffuser. These things considered, the low-frequency amplitude is significantly smaller than that of the blade frequency.

The blade-frequency amplitude value at the high mass-flow rate is greater than that in near-stall mass-flow rate conditions. In addition, the fluctuation is dominated by the blade frequency and its frequency multiplication; substantial low-frequency fluctuations exist at the near-stall mass-flow rate, which is not observed at the high mass-flow rate.

Figure 19 describes six monitoring points position in the volute of the centrifugal compressor. A circle of monitoring points (D1, D2, D3, D4, D5, and D6) are measured inside the volute along the flow direction. Figure 20 plots the amplitude spectrum of the monitoring points of the volutefor one circumferential turn at two different mass-flow rates.

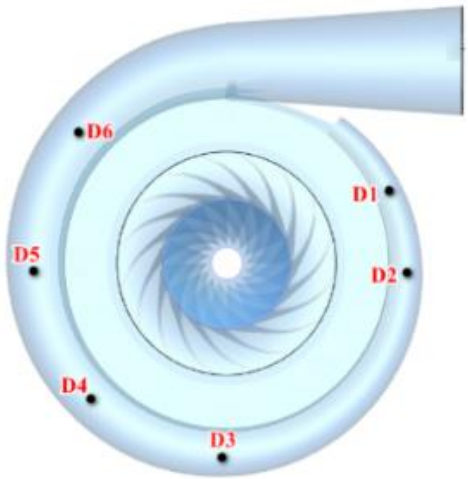

Figure 19. Monitoring points in the volute.

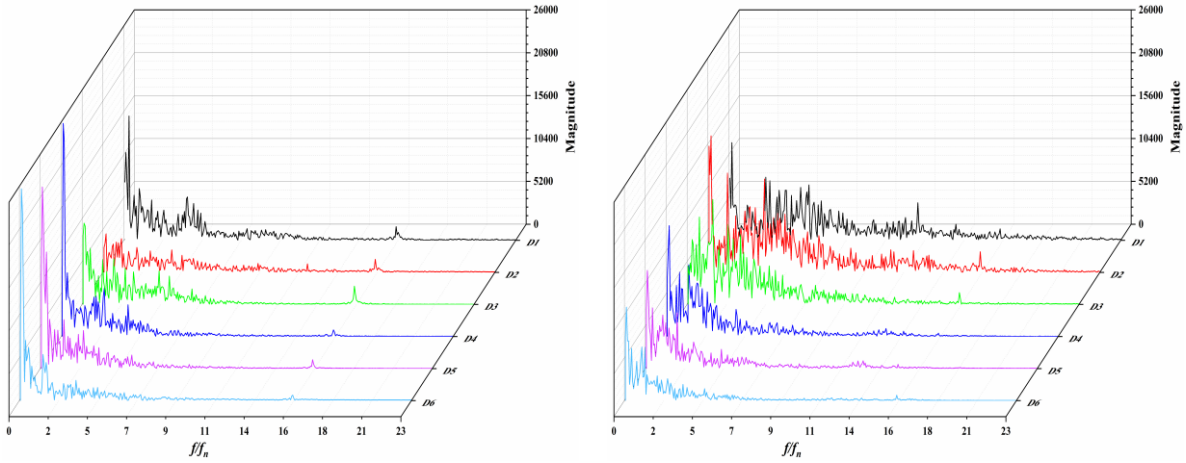

(**a**) 30.46 kg/s (**b**) 22.62 kg/s

Figure 20. Amplitude spectrum of monitoring points in the volute of centrifugal compressor.

In Figure 20, the characteristic frequencies of monitoring points' amplitude spectra are shown to be low at these two mass-flow rates, while the blades' passing frequencies increase. Additionally, the low-frequency amplitude value is significantly larger than that of the blade-frequency amplitude. The low characteristic frequency amplitude at the high mass-flow rate is higher than that at the near-stall mass-flow rate. The amplitude at the near-stall condition is higher than that at the high mass-flow rate from points D1 to D3. It is worth nothing that the amplitude spectrum from points D1 to D3 is more complex, which is caused by the jet-wake in the vaneless diffuser.

4. Conclusions

The internal flow characteristics of the high mass-flow rate and the near-stall mass-flow rate (0.8 Qn = 22.62 kg/s) are studied in a centrifugal compressor with vaneless diffuser by steady and unsteady numerical simulations in this work. Internal flow transitions of the centrifugal compressor are investigated under off-design conditions. Moreover, the internal flow mechanism of centrifugal compressors is analyzed by deviating from the design's operating parameters.

(1) There are obvious differences in the blocking mechanism of the centrifugal compressor at two different mass-flow rates. Excessive velocity is obtained in the impeller at a high mass-flow rate. Furthermore, the excessive velocity gradient at the impeller outlet caused the existence of low-velocity areas and eddies near the tongue, resulting in the blockage of the centrifugal compressor. Backflow is clearly observed in the tip gap at the near-stall mass-flow rate (0.8 Qn). The development of secondary flow is observed in the impeller by boundary-layer separation in the channels. The excessive velocity gradient is generated at the connection between the impeller outlet and the vaneless diffuser, which forms jet-wake structures.

(2) At the high mass-flow rate (1.1 Qn = 30.46 kg/s), some large-scale eddies at the tongue are transformed into small-scale ones which develop turbulence with time evolution.

(3) In the impeller, the near-stall mass-flow rate flow (0.8 Qn) deterioration occurs earlier. Additionally, the high mass-flow rate (1.1 Qn) starts around 50% blade height, while a low mass-flow rate around 30% blade height. The stall frequency is 21.2 Hz and 31.8 Hz at high and low mass-flow rates, respectively. The same characteristic frequencies are shown at the two mass-flow rates: 3.014 fn (1.1 Qn) and 1.989 fn (0.8 Qn), respectively. However, the amplitude of the near-stall mass-flow rate (0.8 Qn) has ahigher peak than that of the high mass-flow rate (1.1 Qn).

(4) For the amplitude spectrum of the vaneless diffuser and volute, the fluctuation of the high mass-flow rate (1.1 Qn) is in the large amplitude, while in the case of the low mass-flow rate, plenty arein the low frequency. The magnitude of these fluctuations

increase due to jet-wakes. Stall frequency is dominant in both conditions, but the difference is that blade frequency is observed at the high mass-flow rate (1.1 Qn).

Author Contributions: Y.W. and K.X. conceived and designed thennumeral calculations; H.Y. and Z.W. analyzed the data; K.X. wrote the paper. All authors have read and agreed to the published version of the manuscript.

Funding: This work was supported by the National Natural Science Foundation of China (11872337, and 11902291), Natural Science Foundation Key Projects of Zhejiang Province (LZ22E060002), the Science and Technology Plan Project of Zhejiang Province (LGG21E060003), and the Science and Technology Key Plan Project of Zhejiang Province (2021C01049, 2020C04011).

Data Availability Statement: The study did not report any data.

Conflicts of Interest: The authors declare no conflict of interest.

References

1. Fowler, H.S. The Distribution and Stability of Flow in a Rotating Channel. *J. Eng. Power* **1968**, *90*, 229–235. [CrossRef]
2. Iwakiri, K.; Furukawa, M.; Ibaraki, S.; Tomita, I. Unsteady and Three-Dimensional Flow Phenomena in a Transonic Centrifugal Compressor Impeller at Rotating Stall. In *Turbo Expo: Power for Land, Sea, and Air.*; ASME: New York, NY, USA, 2009; Volume 48883, pp. 1611–1622. [CrossRef]
3. Kim, C.; Son, C. Comparative Study on Steady and Unsteady Flow in a Centrifugal Compressor Stage. *Int. J. Aerosp. Eng.* **2019**, *2019*, 9457249. [CrossRef]
4. Jenny, P.; Bidaut, Y. Experimental Determination of Mechanical Stress Induced by Rotating Stall in Unshrouded Impellers of Centrifugal Compressors. *J. Turbomach.* **2017**, *139*, 031011. [CrossRef]
5. Tomita, I.; Ibaraki, S.; Furukawa, M.; Yamada, K. The Effect of Tip Leakage Vortex for Operating Range Enhancement of Centrifugal Compressor. In *Turbo Expo: Power for Land, Sea, and Air*; ASME: New York, NY, USA, 2012; Volume 44748, pp. 735–743. [CrossRef]
6. Cao, T.; Kanzaka, T.; Xu, L.; Brandvik, T. Tip Leakage Flow Instability in a Centrifugal Compressor. *J. Eng. Gas Turbines Power* **2021**, *143*, 041012. [CrossRef]
7. Dodds, J.; Vahdati, M. Rotating Stall Observations in a High Speed Compressor—Part II: Numerical Study. *J. Turbomach.* **2015**, *137*, 051003. [CrossRef]
8. Fujisawa, N.; Ohta, Y. Transition Process from Diffuser Stall to Stage Stall in a Centrifugal Compressor with a Vaned Diffuser. *Int. J. Rotating Mach.* **2017**, *2017*, 2861257. [CrossRef]
9. Pascale, K.; Cedric, D. Numerical simulation of unsteady blade row interactions induced by passing wakes. *Eur. J. Mech.* **2006**, *25*, 379–392.
10. Everitt, J.N.; Spakovszky, Z.S. An Investigation of Stall Inception in Centrifugal Compressor Vaned Diffuser. *J. Turbomach.* **2012**, *135*, 011025. [CrossRef]
11. Frigne, P.; Van Den Braembussche, R. Distinction Between Different Types of Impeller and Diffuser Rotating Stall in a Centrifugal Compressor With Vaneless Diffuser. *J. Eng. Gas Turbines Power* **1984**, *106*, 468–474. [CrossRef]
12. Ge, M.; Zhang, G.; Petkovšek, M.; Long, K.; Coutier-Delgosha, O. Intensity and regimes changing of hydrodynamic cavitation considering temperature effects. *J. Clean. Prod.* **2022**, *338*, 130470. [CrossRef]
13. Ge, M.; Petkovšek, M.; Zhang, G.; Jacobs, D.; Coutier-Delgosha, O. Cavitation dynamics and thermodynamic effects at elevated temperatures in a small Venturi channel. *Int. J. Heat Mass Transf.* **2021**, *170*, 120970. [CrossRef]
14. Ge, M.; Manikkam, P.; Ghossein, J.; Subramanian, R.K.; Coutier-Delgosha, O.; Zhang, G. Dynamic mode decomposition to classify cavitating flow regimes induced by thermo-dynamic effects. *Energy* **2022**, *254*, 124426. [CrossRef]
15. Johnson, M.W.; Moore, J. Secondary Flow Mixing Losses in a Centrifugal Impeller. *J. Eng. Power* **1983**, *105*, 24. [CrossRef]
16. Greitzer, E.M. Surge and Rotating Stall in Axial Flow Compressors—Part II: Experimental Results and Comparison With Theory. *J. Eng. Power* **1976**, *98*, 199–211. [CrossRef]
17. Moore, F.K.; Greitzer, E.M. A Theory of Post-Stall Transients in Axial Compression Systems: Part I—Development of Equations. *J. Eng. Gas Turbines Power* **1986**, *108*, 68–76. [CrossRef]
18. Garnier, V.H.; Epstein, A.H.; Greitzer, E.M. Rotating Waves as a Stall Inception Indication in Axial Compressors. *J. Turbomach.* **1991**, *113*, 290–301. [CrossRef]
19. Spakovsky, Z.S. Backward Traveling Rotating Stall Waves in Centrifugal Compressors. *J. Turbomach.* **2004**, *126*, 1–12. [CrossRef]
20. Pullan, G.; Young, A.M.; Day, I.J.; Greitzer, E.M.; Spakovszky, Z.S. Origins and Structure of Spike-Type Rotating Stall. *J. Turbomach.* **2015**, *137*, 051007. [CrossRef]
21. Mischo, B.; Jenny, P.; Mauri, S.; Bidaut, Y.; Kramer, M.; Spengler, S. Numerical and Experimental Fluid–Structure Interaction-Study to Determine Mechanical Stresses Induced by Rotating Stall in Unshrouded Centrifugal Compressor Impellers. *J. Turbomach.* **2018**, *140*, 111006. [CrossRef]

22. Li, D.; Zhang, N.; Jiang, J.; Gao, B.; Alubokin, A.A.; Zhou, W.; Shi, J. Numerical investigation on the unsteady vortical structure and pressure pulsations of a centrifugal pump with the vaned diffuser. *Int. J. Heat Fluid Flow* **2022**, *98*, 109050. [CrossRef]
23. Day, I.J. Stall, Surge, and 75 Years of Research. *J. Turbomach.* **2015**, *138*, 011001. [CrossRef]
24. Du, Y.; Dou, H.-S.; Lu, F. Counter-Propagating Rotating Stall of Vaned Diffuser in a Centrifugal Compressor Near Design Condition. *J. Turbomach.* **2020**, *142*, 111007. [CrossRef]
25. Lateb, M.; Masson, C.; Stathopoulos, T.; Bédard, C. Comparison of various types of k–ε models for pollutant emissions around a two-building configuration. *J. Wind. Eng. Ind. Aerodyn.* **2013**, *115*, 9–21. [CrossRef]
26. Shahin, I.; Gadala, M.; AlQaradawi, M.; Badr, O. Large Eddy Simulation for a Deep Surge Cycle in a High-Speed Centrifugal Compressor With Vaned Diffuser. *J. Turbomach.* **2015**, *137*, 101007. [CrossRef]
27. Smagorinsky, J. General circulation experiments with the primitive equations. *Mon. Weather. Rev.* **1963**, *91*, 99–164. [CrossRef]
28. Speziale, C.G.; Erlebacher, G.; Zang, T.A.; Hussaini, M.Y. The subgrid-scale modeling of compressible turbulence. *Phys. Fluids* **1988**, *31*, 940. [CrossRef]
29. Elias, S.; Mihai, M.; Marco, G. Analysis of Vaneless Diffuser Stall Instability in a Centrifugal Compressor. *Int. J. Turbomach. Propuls. Power* **2017**, *2*, 19.
30. Hellstrom, F.; Gutmark, E.; Fuchs, L. Large Eddy Simulation of the Unsteady Flow in a Radial Compressor Operating Near Surge. *J. Turbomach.* **2012**, *134*, 051006. [CrossRef]
31. Liu, Y.; Liu, B.; Lu, L. Investigation of Unsteady Impeller-Diffuser Interaction in a Transonic Centrifugal Compressor Stage. *Turbo Expo Power Land SeaAir* **2010**, *44021*, 1961–1971. [CrossRef]
32. Sundström, E.; Semlitsch, B.; Mihăescu, M. Generation Mechanisms of Rotating Stall and Surge in Centrifugal Compressors. *Flow, Turbul. Combust.* **2017**, *100*, 705–719. [CrossRef]
33. Lou, F.; Fabian, J.C.; Key, N.L. Stall Inception in a High Speed Centrifugal Compressor During Speed Transients. *J. Turbomach.* **2017**, *139*, 121004.1–12100410. [CrossRef]
34. Guo, Q.; Chen, H.; Zhu, X.-C.; Du, Z.-H.; Zhao, Y. Numerical simulations of stall inside a centrifugal compressor. *Proc. Inst. Mech. Eng. Part A J. Power Energy* **2007**, *221*, 683–693. [CrossRef]